Fizika Nizkikh Temperatur, 2003, v. 29, No. 3, p. 270–285

Reactions induced by low energy electrons in cryogenic films

(Review Article)

Andrew D. Bass and Leon Sanche*

Department of Nuclear Medicine and Radiobiology, University of Sherbooke
Sherbooke, Quebec, I1H5N4, Canada
E-mail: Andrew.Bass@Usherbrooke.ca

Received December 13, 2002

We review recent research on reactions (including dissociation) initiated by low-energy electron bombardment of monolayer and multilayer molecular solids at cryogenic temperatures. With incident electrons of energies below 20 eV, dissociation is observed by the electron stimulated desorption (ESD) of anions from target films and is attributed to the processes of dissociative electron attachment (DEA) and to dipolar dissociation. It is shown that DEA to condensed molecules is sensitive to environmental factors such as the identity of co-adsorbed species and film morphology. The effects of image-charge induced polarization on cross-sections for DEA to CH_3Cl are also discussed. Taking as examples, the electron-induced production of CO within multilayer films of methanol and acetone, it is shown that the detection of electronic excited states by high resolution electron energy loss spectroscopy can be used to monitor electron beam damage. In particular, the incident energy dependence of the CO indicates that below 19 eV, dissociation proceeds via the decay of transient negative ions (TNI) into electronically excited dissociative states. The electron induced dissociation of biomolecular targets is also considered, taking as examples the ribose analog tetrahydrofuran and DNA bases adenine and thymine, cytosine and guanine. The ESD of anions from such films also show dissociation via the formation of TNI. In multilayer molecular solids, fragment species resulting from dissociation, may react with neighboring molecules, as is demonstrated in anion ESD measurements from films containing O_2 and various hydrocarbon molecules. X-ray photoelecton spectroscopy measurements reported for electron irradiated monolayers of H_2O and CF_4 on a Si–H passivated surface further show that DEA is an important initial step in the electron-induced chemisorption of fragment species.

PACS: 79.20.La, 82.30.Lp

1. Introduction

The interactions of electrons of energies less than ~20 eV with the constituent atoms and molecules of condensed matter are of considerable interest since low energy electrons generated within and at the surface of condensed media are implicated in a variety of processes ranging from the aging of dielectrics under high voltage [1], friction induced damage to lubricants [2] and nano-lithography (for example see [3]). Interest also lies in their use to study catalytic reaction intermediates by their dissociative interaction with organic molecules [4]. Motivation for the authors' research derives essentially from the large numbers of low energy secondary electrons generated within biological systems by irradiation with high energy primary particles (e.g., therapeutic x-rays) [5]. What role (if any) do these secondary electrons play in the genotoxic effects of radiation? Attempting to answer this question, we have adapted techniques from gas-phase electron-scattering experiments for use with thin solid targets. In a typical experiment an energy-selected beam of electrons is incident from vacuum on to a solid film and a variety of analytical techniques are then used to determine the mechanisms by which electronic energy is absorbed. These techniques may include surface spectrocopies, such as high resolution electron energy loss (HREELS), x-ray pho-

* Canada Chair in the Radiation Sciences

© Andrew D. Bass and Leon Sanche, 2003

toelectron spectroscopy (XPS) or measurements of particle desorption or of charge accumulation within the film. Experimental systems studied include simple vapor deposited atomic and molecular solids, molecules physisorbed on ordered metal and semiconductor surfaces, organic self-assembled monolayers and complex bio-molecules such as DNA. Various aspects of this work, as applied to dielectric aging [1], electron microscopy [6], radiation track calculations [7] and particle desorption [8] have been described elsewhere. Here we will discuss principally results reported within the past 6 years that demonstrate electron-induced chemical changes, including dissociation, in condensed phase systems. As a further restriction on our discussion, all the target systems presented, whether thin molecular solids or adsorbate/substrate systems, require cryogenic stabilization. We stress that while cooling to temperatures of between 15 K and 100 K allows preparation of films under ultra-high vacuum (UHV) conditions, cryogenic conditions also limit vibrational excitation of the molecular constituents in the solid targets and help ensure that the observed electron-scattering effects are dominated by the interaction of electrons with the majority of molecules in their vibrational ground-state.

The structure of this paper is as follows: In Sec.2, we introduce various theoretical concepts, such as negative ion resonances, which are required to explain low energy electron-scattering in condensed matter. In Sec. 3, we briefly describe the experimental methods. In Sec. 4, we present recent results on electron-induced dissociation in several systems including, condensed halomethanes, acetone and methanol and simple organic molecules of biological significance. In Sec. 5, we discuss simple reactions, including ion scattering, that succeed electron induced dissociation.

2. Electron-scattering phenomena

Studies of electron–molecule scattering and attachment in the gas phase have a long history, dating back to the experiments of James Franck and Gustav Hertz in 1914 [9]. Subsequent research has shown how at low energies (i.e., below ~20 eV), cross sections for electron-molecule scattering are often dominated by the transient localization of the electron on the molecule, in what is often termed a «resonance» [10]. (It is likely that the striking clarity of the original Franck–Hertz experiment owes much to excitation of a resonance near the threshold of the 6^3P states of mercury [11].) From an atomic and molecular orbital perspective, resonances can be considered as temporary or transient negative ions and may be classed as belonging to one of two broad types. If the additional electron occupies a previously unfilled orbital of the target in its ground state, the transitory state is referred to as a *single particle resonance*. The term «*shape resonance*» applies more specifically, when temporary trapping of the electron is due to the shape of the electron-molecule potential. When electron capture is accompanied with electronic excitation, so that two electrons occupy previously unfilled orbitals, the resonance is called «*core-excited*».

The prevalence of resonances in gas-phase electron-molecule collisions and the universal nature of the short-range interactions responsible for their formation have suggested that similar phenomena should exist at higher levels of aggregation in condensed matter. Indeed, experimental studies performed in our laboratory over the past 20 years have consistently shown that electron scattering with condensed molecules is strongly modulated by the formation transient negative ions. However, and contrary to the gas-phase where the captured electron must remain attached to a single atom or molecule throughout its lifetime, in solids the transient anion can hop between adjacent sites via inter-atomic or inter-molecular electron transfer [12]. For motion to occur in the case of core-excited resonances, three electrons must be involved in the process [12], e.g., a two-electron transition accompanied by an electron transfer. Such electron and energy transfer leads to the formation of a transient anion having a specific wave-vector in the lattice or at the surface and may be referred to as an «electron-exciton complex»[13].

When an electron resonance occurs, the temporary capture of an electron at an atomic or molecular site increases the interaction time of the electron at that site in proportion to the resonance lifetime ($\tau_a \sim 10^{-16} - 10^{-13}$s) and the inverse of the electron transfer rate. This local interaction causes a distortion of the atom (or molecule) that accepts the additional electron, multipole forces. One product of this fundamental interaction, of great relevance to the experimental systems discussed in this article is dissociative electron attachment (DEA), which arises essentially from the molecular distortion.

Dissociative electron attachment occurs when the molecular transient anion state is dissociative in the Franck–Condon (FC) region, the localization time is of the order of, or larger than the time required for dissociation along one nuclear coordinate and one of the resulting fragments has positive electron affinity. In this case, a stable atomic or molecular anion is formed along with one or more neutral species. This process is analogous to the well-known Menzel – Gomer – Redhead model of desorption via a FC electronic transition to a repulsive state [14]. DEA usually occurs via the formation of core-excited reso-

nances, since these possess sufficiently long lifetimes to allow for dissociation of the anion before autoionization. Hence, when surface molecules are bombarded with a low-energy (0–20 eV) electron beam, a portion of the neutral and anionic species formed by DEA can desorb.

Within a local complex potential curve crossing model, the cross section for the simple DEA reaction $e + AB \rightarrow AB^- \rightarrow A^- + B$, where AB is a diatomic molecule, may be expressed as [15]

$$\sigma_{DEA}(E) = \sigma_{\text{cap}}(E) P_s \tag{1}$$

where P_s represents the survival probability of the anion against autodetachment of the electron and E the incident electron energy. The capture cross section σ_{cap} is given by

$$\sigma_{\text{cap}}(E) = \lambda g |\chi_\upsilon|^2 \left[\frac{\Gamma_a}{\Gamma_d}\right] \tag{2}$$

where λ is the de Broglie wavelength of the incident electron, g is a statistical factor, and χ_υ is the normalized vibrational nuclear wave function. Γ_a is the *local* energy width of the AB^- state in the FC region, and Γ_d is the *extent* of the AB^- potential in the FC region. The width of the transient anion state in the autodetaching region defines the lifetime τ_a towards autodetachment, $\tau_a(R) = \hbar/\Gamma_a(R)$, such that the survival probability of the temporary anion, after electron capture, is given by

$$P_s = \exp\left[-\int_{R_E}^{R_c} \frac{dt}{\tau_a(R)}\right] \tag{3}$$

where R_E is the bond length of the anion at energy E and R_c is that internuclear separation beyond which autodetachment is no longer possible. If we define an average lifetime $\overline{\tau}_a$ and let $K \equiv \lambda g |\chi_\upsilon|^2$, then Eq. (1) becomes

$$\sigma_{DEA}(E) = K\left[\frac{\Gamma_a}{\Gamma_d}\right] \exp\left[-\frac{\overline{\tau}_c}{\overline{\tau}_a}\right] \tag{4}$$

Here $\overline{\tau}_c(E) \equiv |R_c - R_E|/v$ where v is the average velocity of separation of the fragments A^- and B upon dissociation. Hence, the DEA cross section depends exponentially on the ratio of the lifetime of the transient anion and the velocities of the fragments. Equation (4) defines most of the *intrinsic* characteristics of the DEA process. It may be seen from this equation, that the magnitude of the DEA signal depends on parameters which are influenced by the nature of the solid target; i.e., the attaching electron wavelength λ, the resonance lifetime $\overline{\tau}_a$ and curve crossing at R_c between the anion state and a neutral state beyond which autodetachment is no longer possible. This aspect of DEA, its sensitivity to environmental factors, will be dealt with in some detail in the following Sections. It is also important to recognize DEA as a mechanism for producing reactive (ionic and neutral) species of non-thermal energies and as such represents an initial step in the more complex reactive pathways induced by low-energy electrons. Examples of such DEA mediated reactions will also be given.

3. Experimental techniques

The experiments described in this article were performed under ultra high vacuum, that is within vacuum chambers evacuated by cryogenic, ion and turbo-molecular pumps to base pressures of between 10^{-11} and 10^{-10} torr. Molecular solid targets are formed by vapor-deposition onto a clean substrate, held at temperatures varying from 15 to 100 K by cryostat. The substrate is usually a polycrystalline metal foil, a Pt monocrystal, or semiconductor crystal which can be cleaned by resistive heating and/or ion bombardment. The condensed films can be grown with either a gas-volume expansion dosing procedure [16] and calibrated by monitoring the quantum size effect features observed in ultra-thin films [17] or for higher molecular mass adsorbates, timed deposition from an oven source.

Once formed, sample films can be probed with a variety of electron beam techniques. Dissociative processes (and certain other reactions) are most effectively detected when a fragment ion or neutral species is desorbed into vacuum. Generally, ion desorption is easier to observe than that for neutral species, since desorbed charged particles can be immediately mass analysed. Figure 1 illustrates schematically an experimental system for ion desorption studies of large organic/biomolecular targets. Note the load-lock section for the introduction of sample slides and/or the degasing of organic molecules within an oven prior to

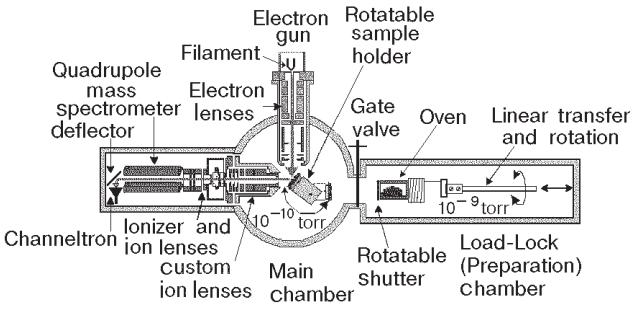

Fig. 1. Schematic overview of an apparatus suitable for measurements of the electron stimulated desorption of anions from vacuum deposited films [18].

their introduction into the analysis chamber. In this instrument, [18], an electron gun produces an electron beam of variable energy having a current of between 5 and 300 nA with an energy resolution of ~ 250 meV full width at half maximum (FWHM). The electron beam is incident on the cryogenically cooled solid target. The electron energy scale is calibrated to within ± 300 meV with respect to the vacuum level $E_{\rm vac}$ by measuring the onset of the current transmitted through the film. Ions desorbed during electron impact enter an ion lens (containing a set of retardation grids) which precedes a quadrupole mass spectrometer. So-called *ion yield functions* are obtained by recording a particular ion signal as a function of incident energy E. In another ESD instrument, the electron gun is replaces with an electrostatic monochromator which produces an electron beam of 2 nA at a resolution of 80 meV [19]. In this latter instrument double μ-metal shields surround the vacuum chamber to eliminate stray magnetic fields.

In principle, the neutral desorbed products of dissociation can be detected and mass analyzed, if ionized prior to their introduction into the mass spectrometer. However, such experiments are difficult due to low *effective* ionization efficiencies for desorbed neutrals. Nevertheless, a number of cryogenic systems have been studied in the groups of Feulner [20], Orlando [21], and Arumainaygam [22], for example. In our laboratory, studies of neutral particle desorption have concentrated on self assembled monolayer targets at room-temperature [23], outside the scope of this review. Under certain circumstances, neutrals desorbed in electronically excited metastable states of sufficient energy can be detected by their de-excitation at the surface of a large-area microchannel plate/detector assembly [24]. Separation of the ESD signal of metastables from UV luminescence can be effected by time of flight analysis [24].

While desorption measurements provide clear evidence of molecular dissociation, quantitative measurements are difficult to perform, due partly to experimental uncertainties (such as the efficiency of ion transmission through the mass spectrometer), but also because only a small, poorly known fraction of ions (or neutrals) desorb. However, quantitative measurements are often possible using a modification of low energy electron transmission (LEET) spectroscopy. In LEET experiments [16], a trochoidal monochromator [25] providing an electron current of between 1 and 10 nA with an intrinsic resolution of between 40 to 60 meV FWHM is incident normally on the film surface. A LEET spectrum is obtained by measuring the current I_t arriving at the substrate as a function of E. Cross sections for electron trapping or stabilization by molecules condensed onto a dielectric film can also be obtained [26,27]. Electronic charge trapped at the surface, following exposure of the film to electrons of a known energy, produces a retarding potential ΔV, which is apparent as a displacement of any subsequent LEET spectrum to higher incident energies. The observed rate of charging A_s (the charging coefficient) can be converted into a charging cross section σ_{CT} as follows:

$$A_s \equiv d\Delta V(t)/dt\Big|_{t=0} = (LI\mu_0/\varepsilon\pi r^2)\,\sigma_{CT} \qquad (6)$$

where L and ε are the spacer layer thickness and dielectric constant, respectively, and μ_0 is the surface density of molecular targets; I and r are the total current and radius of the incident electron beam, respectively. Analysis of errors including those associated with the preparation of the target film, suggest a total error of ± 50% on the absolute values of measured cross sections. Combined with the mass spectrometric measurements of anion ESD, σ_{CT} cross sections can on occasion allow absolute cross sections for DEA to be obtained.

Electron-induced changes in film chemistry can also be observed using surface sensitive techniques such as high resolution electron energy loss (HREEL) spectrocopy [28]. An HREELS spectrometer allows the energy losses of electrons scattered near the surface of thin films and their dependence on incident electron energy to be measured. In addition to the cryogenically cooled substrate [29], such an instrument includes an electron monochromator and an energy analyzer, both of which employ hemispherical electrostatic deflectors to achieve optimal resolution (~ 5 to 30 meV FWHM). Typically, the monochromator produces a focused electron beam that strikes the film surface at an angle θ_0 from the film normal. Electrons scattered in a narrow pencil about angle θ_r relative to the surface normal are energy analyzed with the second hemispherical deflector. Energy loss processes include vibrational and electronic excitations of target atoms and molecules. Energy loss spectra are recorded by sweeping the potential of the monochromator or analyzer relative to the grounded target. The energy dependence of the magnitude of a given loss process (i.e. the excitation function) is obtained by sweeping the energy of both deflectors with the potential difference between them, corresponding to the probed energy.

X-ray photoelectron spectroscopy [30] allows quantitative elemental analysis of thin films and provides information on the chemical states of atoms in molecules. It uses the fact that the kinetic energy KE of a photoelectron emitted from a film under x-ray bombardment (at $h\nu$ = 1254 eV) is related to its bind-

ing energy in the atom from which it came E_B, by the relation $E_B = h\nu - KE$. The kinetic energy, measured with an electrostatic hemispherical analyzer, thus identifies the source atom (and electronic transition) of the photoelectron. Since the binding energies of inner shell electrons are perturbed by chemical bonding, accurate measurements of KE allow the chemical state of an atom to be determined (e.g., E_B of a C (1*s*) electron in CO_2 differs from that of a C (1*s*) electron in CN). The relative intensities of elemental XPS signals relate directly to the elemental concentrations in the sample.

Both HREELS and XPS can thus be used to determine cross sections for the production of particular atomic and molecular species within a film, following electron bombardment. Effective cross sections may then be obtained by measuring the variation of the amplitude of a signal associated with a particular product with the integrated electron current, at specific electron energies.

4. Electron induced dissociation

Below 20 eV, the electron stimalated desorption (ESD) of anions from condensed systems is attributed to DEA, which produces oscillatory structures in the anion yield functions, and to dipolar dissociation (DD), which produces both anionic and cationic fragments. Typically, DD produces as a featureless signal which increases linearly with electron energy from a threshold lying between 10 and 20 eV. Anion desorption data is often dominated by the DEA process. The first observations of DEA in a solid were made from the ESD of O^- from multilayer O_2 films [31]. Subsequently, the O_2 molecule has served as a model target to study factors affecting the physics of DEA in condensed phase systems [6].

The yield of O^- from electron impact on gas phase and multilayer condensed O_2 is shown in Fig. 2,*a* and 2,*b*, respectively. In the gas phase, the O^- signal is dominated by DEA via the $^2\Pi_u$ state of O_2^- at ~ 6.7 eV [32]. In contrast, the anion yield function from multilayer O_2 shows in addition to DD above ~ 15 eV, a much broader resonance feature between 5 and 10 eV, and a further structure at 13 eV. Both the «broadening» of the lower energy structure and the appearance of the 13 eV structure are attributed to a relaxation of the $\Sigma^- \leftrightarrow \Sigma^+$ selection rule that occurs when the cylindrical symmetry of the molecular wave function is broken by adjacent molecules. The new structures thus correspond to DEA via Σ^+ states between 8 and 10 eV and at 13.5 eV [33].

Also shown in Fig. 2 (c–*g*) are the anion yield functions for sub-monolayer quantities of O_2 deposited onto various multilayer atomic and molecular solids.

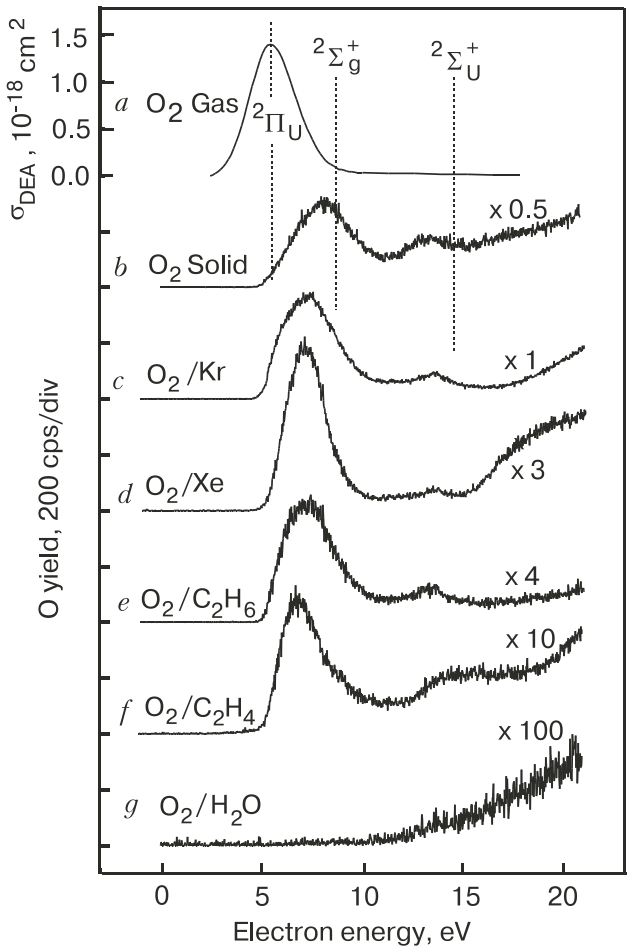

Fig. 2. O^- yield functions for electron impact on gaseous O_2 (*a*), 4 monolayers (ML) of O_2 (*b*) and 0.15 ML of O_2 condensed on 4 ML of the indicated substrate (*c*–*g*). The dashed lines and bars indicate the known positions of the O_2^- resonances. The gain factor over each curve is relative to curve (*c*), and the shifted baselines correspond to the zero anion intensity levels. Figure based on the data of Ref. 19.

The data represents part of a study [19] on the environmental factors involved in the DEA process. As can be seen, the yield of desorbed ions can vary greatly with substrate composition. These variations were largely attributed to so-called *extrinsic factors* that modify the ESD process at times before attachment and after dissociation, for example electron energy loss processes in the substrate and post-dissociation interactions (PDI) of ions with the surrounding medium. Such processes can be contrasted with *intrinsic factors,* which modify the properties of the resonance (e.g., lifetime, energy, decay channels). In general, the O^- yields per O_2 molecule are higher for O_2 deposited on rare gas solids Kr and Xe (Fig. 2,*c* and 2,*d*, — see [34] for detailed comparison of O^- desorption from rare gas solids) than on a molecular solids where extrinsic effects such as electron energy loss processes and PDI are more likely. The weakest

O^- signal was observed from O_2 on H_2O, (Fig. 2,*g*) which like the other substrate films was condensed at a temperature of 20 K. The figure shows that while the DD signal is reduced by approximately a factor of 100 relative to O_2 on Kr, the O^- ESD signal over the energy range associated with DEA is almost entirely absent. Initially this dramatic effect (termed *quenching*) was attributed to some interaction of the transient O_2^- states with the dipole moment of the adjacent water molecules. However, later work [35,36] has shown that amorphous water films formed at 20 K can be highly porous. When O_2 is deposited onto porous ice at 20 K (close to the sublimation temperature of oxygen), it diffuses rapidly over the film's extended surface, so that the effective density of O_2 at the film vacuum interface is lowered considerably from that obtained when the same quantity is deposited onto a non-porous film. Oxygen ions formed inside the film have a much lower probability of desorption than those generated at the film/vacuum since they are more likely to scatter and lose kinetic energy [37]. Thus, the signal of desorbed ions derives primarily from DEA to O_2 adsorbed at the film vacuum interface and since the number of these latter has been reduced, the desorption signal drops similarly. Nevertheless, comparisons of O^- ions from O_2 on porous water and benzene films [38] demonstrate that the effects diffusion alone are insufficient to explain the startling diminution of signal evidences in Fig. 2,*g* which must therefore derive from a combination of other factors.

The incident-electron energy dependence of the surface charging cross section σ_{CT} for 0.1 ML of CH_3Cl condensed onto a 15-ML Kr film [39,40] is shown in Fig. 3,*a*. The two curves (*b*) and (*c*) show the H^- and Cl^- ESD yield functions for similar quantity of CH_3Cl deposited onto a 7-ML Kr film [41]. No ESD signal was detected below 5 eV. Curve (*d*) in Fig. 3 is the total anion yield from the gas phase as measured by Pearl and Burrow [42], and was obtained by subtracting a background signal at 0 eV arising from CCl_4. The 0.8 eV peak in this curve represents a cross section of $(2.0 \pm 0.4)\cdot 10^{-21}$ cm^2 for anion production, much smaller than the value of $(13 \pm 2)\cdot 10^{-18}$ cm^2 for the 0.5 eV peak in Fig. 3,*a*. Moreover, the origin of this gas phase structure has been questioned, as its variation of magnitude with increasing temperature is consistent with the DEA of HCl [42].

The variation with Kr film thickness of the amplitude (full squares) and energy at maximum (open squares) of the lowest energy charge trapping cross section feature is shown in Fig. 4. It is apparent that both these quantities are strongly dependent on Kr film thickness. The thickness dependence of the feature's energy, is reminiscent of that observed by Michaud and Sanche [43] in the energy of the $^2\Pi_g$ resonance of N_2 on Ar, which was successfully described in terms of the polarizability of the Ar film and the image-charge induced in the metal substrate. The lower dashed curve fit to the data uses the same type of function used by Michaud and Sanche to describe the thickness dependent changes in polarization energy V_p [43].

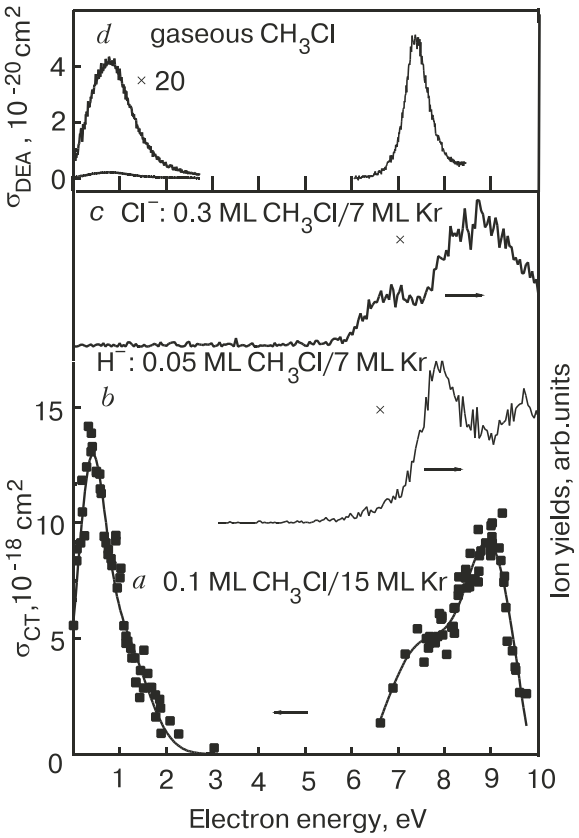

Fig. 3. Charging cross section and anion yields induced by 0–10 eV electron impact on CH_3Cl. (*a*) Absolute surface charging cross section for 0.1 ML methyl chloride condensed on a 15 ML Kr film. (*b*) H^- and Cl^- desorption yields from Ref. 41. (*c*) Total anion yield from gaseous methyl chloride from [42]. Figure taken from Ref. 40.

The structure near 0.5 eV in Fig. 3,*a* has been interpreted [39,40] as due to the formation of Cl^- anions via DEA to the $^2A_1$ state of CH_3Cl^- and the subsequent dissociation of Cl^- and CH_3 along the strongly antibonding $C-Cl^-$ σ^* orbital. Since no ESD signal is observed in Fig. 3,*b* and 3,*c* below 5 eV, the charge trapping cross section represents an absolute DEA cross section at these low energies. The value reported for CH_3Cl on a 5 ML thick Kr film (Fig. 4) thus represents an enhancement over gas-phase experimental [42] and theoretical values [44] of between 4 and 6 orders of magnitude, respectively. This remarkable enhancement has been attributed to image-charge in-

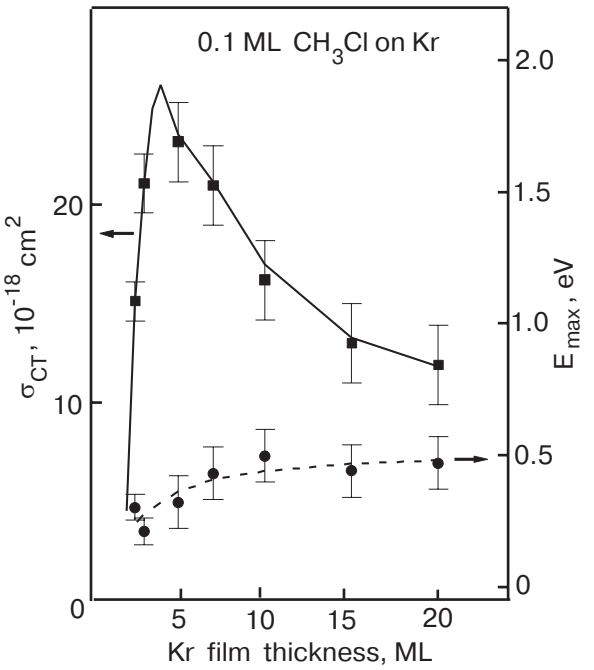

Fig. 4. Variation of maximum σ_{CT} with Kr film thickness for low-energy electrons incident on 0.1 ML of CH_3Cl deposited on the surface of Kr films. The solid line drawn from the data represents the results of an R-matrix calculation to describe electron-CH_3Cl/Kr scattering. Variation in energy E_{max} of the maximum in σ_{CT} with Kr film thickness. Dashed line is a parametric fit to E_{max} using the image charge model of [43]. Experimental data taken from Ref. 39.

duced polarization energy which lowers the potential energy curve of the intermediate transient anion [39]. Similarly, when charging measurements were performed for CH_3Cl molecules sandwiched between Kr layers of variable thickness, where V_p is larger, a further increase of approximately a factor 10 in DEA cross section was reported [45].

The process can be qualitatively understood by reference to Fig. 5, which shows idealized potential energy *PE* curves for ground state CH_3Cl and the $^2A_1$ state of CH_3Cl^- along the C–Cl coordinate. In the gas-phase, the $^2A_1$ anion state (the dash-dotted curve in Fig. 5,*a*) lies at resonance energy E_R = 3.45 eV above the neutral ground state in the Franck–Condon region, represented in the figure by the extent of Gaussian-like nuclear wave-function. The lifetime is considered too short to allow dissociation of the molecule (the extra electron autodetaches at separations $< R_c$ the crossing point of the anion and neutral curves) but is sufficient to initiate vibrational excitation (panel *b*) centered at E_R. Upon condensation, the isolated anion's curve is lowered by V_p, to give the *PE* curve for the molecule on the Kr surface (the dashed curve in panel *a*). The energy of vibrational excitation also shifts by V_p, to a new resonance energy E'_R. Now, the new crossing point R'_c of anion and neutral curves, is much closer to the Franck–Condon region so reduc-

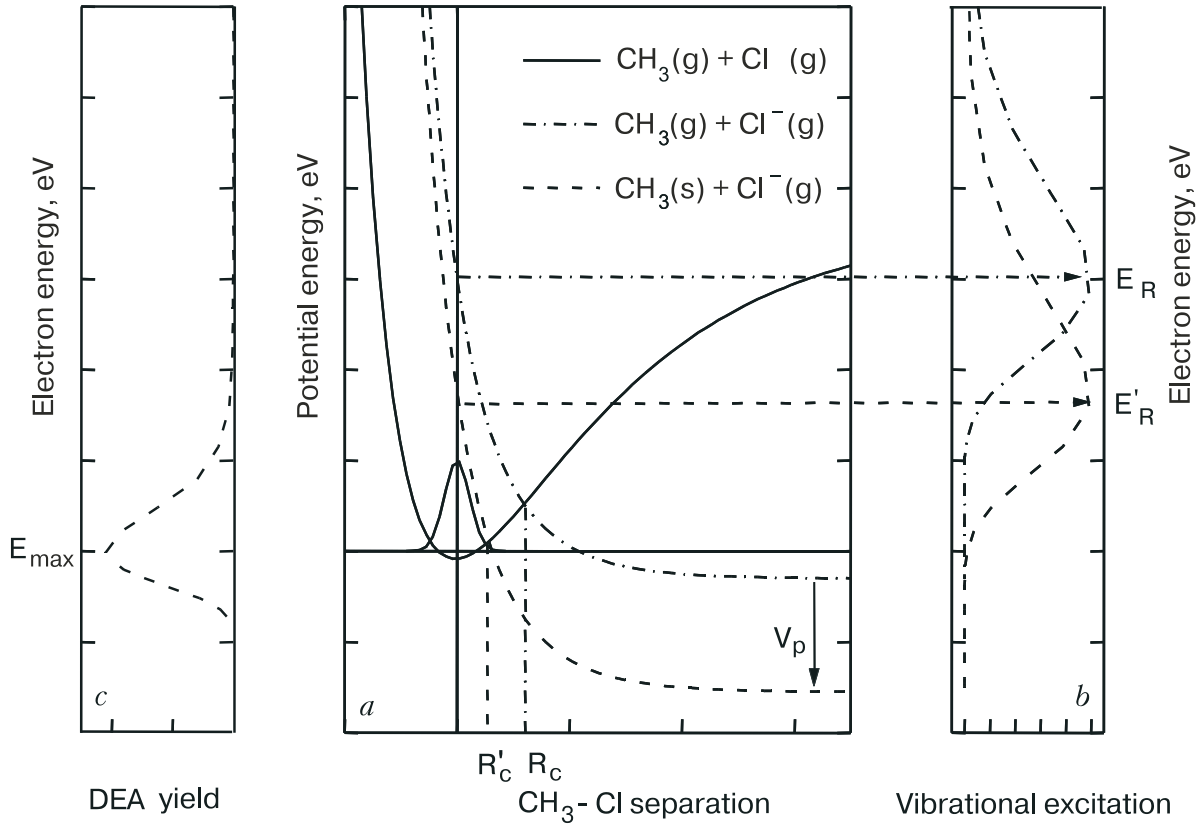

Fig. 5. Effect of polarization energy V_p on (*a*) potential energy curves of transient CH_3Cl state. (*b*) Vibration excitation function and (*c*) DEA yield function. See text for details.

ing the time (and distance) required to dissociate. Some anions thus survive auto-detachment to achieve dissociation, but since the process will still favour anions formed at inter-nuclear separations close to R_c', the maximum in the DEA yield and charge trapping cross section appear at $E_{\max} < E_R'$ (panel *c*). The DEA yield is further enhanced by an increase in anion lifetime that accompanies any decrease in resonance energy as evidenced by changes in the DEA yield of Cl^- ions from gas-phase chloroalkane molecules [46].

A more quantitative understanding of the effect of V_p on electron attachment to CH_3Cl adsorbed on Kr [39,40] and within its bulk [45] has been attempted using a modified version of the R-matrix scattering model [44] used with success to describe low energy electron-CH_3Cl scattering in the gas-phase [47]. Essentially the model was modified to include the effects of V_p at short electron-molecule distances. The solid line in Fig. 4 represents the results of the R-matrix calculation. However, to obtain this result it was also necessary to model in semi-empirical fashion the electron's interaction with the metal substrate. The discontinuity represented by the film's surface complicates considerably this type of calculation, which is more straight-forward for CH_3Cl embedded within bulk Kr. In this case, [45] good agreement between theory and experiment is possible by adjusting V_p alone. However, it must be noted that the values of V_p required to fit the data for CH_3Cl condensed on and within Kr, are approximately 50% larger than those measured elsewhere for Kr films [43]. If these latter values are used, the calculated cross sections are about one order of magnitude too small. This disparity is not the case when comparing similar charging data for CF_3Cl [48] with an R-matrix calculation [49]. Comparison of the CH_3Cl and CF_3Cl data and calculations [49] suggest the CH_3Cl^- *PE* curve may be modified in the Kr environment due to a change of symmetry and/or screening of the CH_3 and Cl^- interaction by the Kr medium at intermediate inter-nuclear separations. Alternatively, Aflatooni and Burrow have suggested that the effective polarization energy seen by CH_3Cl on Kr could indeed be larger than that measured for N_2^- on Kr [43] due to the larger static dipole moment of this molecule.

High resolution electron energy loss measurements

In two recent papers Lepage, Michaud, and Sanche [50,51] have demonstrated the use of HREELS to measure *in situ* the neutral dissociation products arising from the impact of low energy electrons on thin physisorbed multilayer films. The technique is similar to that developed earlier by Martel et al. [52], since a single electron beam is used for both the production

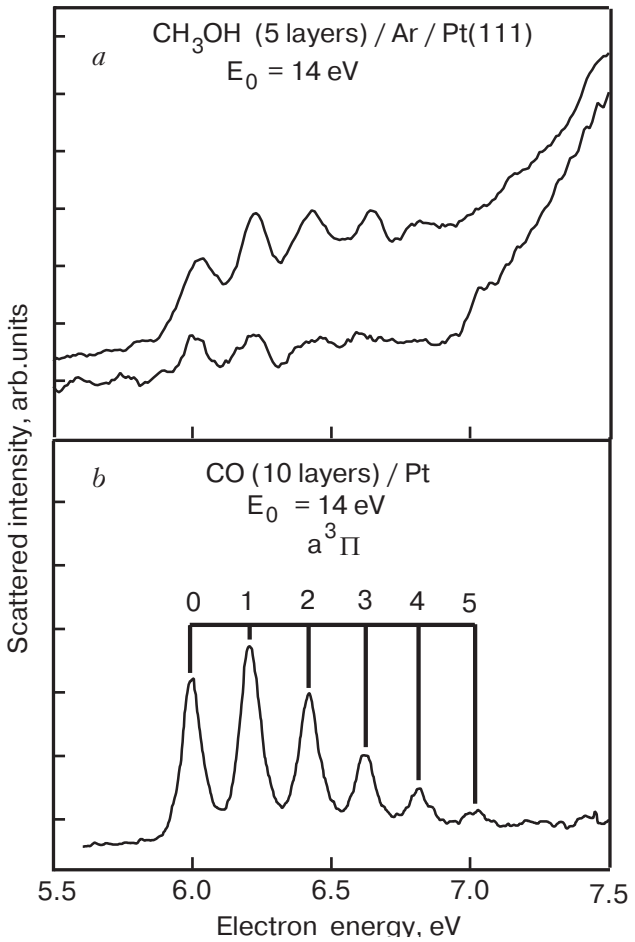

Fig. 6. Electron-energy-loss spectra with 14-eV electrons incident on: (*a*) a 5-layers film of methanol condensed on an Ar spacer after exposition to small (lower curve) and large (higher curve) electron doses and (*b*) a 10-layers film of CO condensed on a platinum substrate. The $a^3\Pi$ excited state of CO is characterized by a vibrational progression having a spacing of about 0.21 eV [50].

and detection of the neutral fragments. However, in the experiments of Lepage et al., the neutrals are detected via their electronic excitations, rather than by the spectroscopy of their vibrational levels. This is particularly advantageous in the study of hydrocarbon targets, which often have many strong vibrational losses, that can obscure those of the products. Figure 6,*a* shows HREEL spectra of multilayer methanol (CH_3OH) for energy losses in the range 5.5 to 7.5 eV. The incident electron energy was 14 eV. The lower curve in Fig 6,*a* was taken after 5 mins of electron bombardment of the CH_3OH film. Weak structure is visible in the spectrum at energies below 6.7 eV. The upper curve was recorded after 20 mins of exposure to the 14 eV electron beam and shows the evolution of the weak structures into a series of sharp peaks. These peaks corresponds almost exactly to the vibrational progression in the lowest electronic state

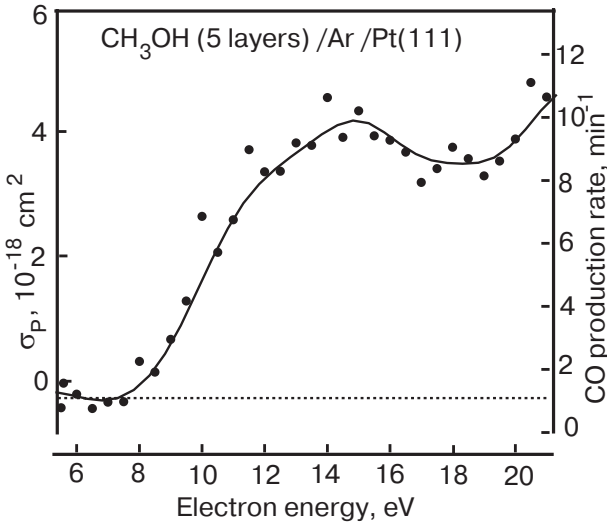

Fig. 7. Electron total scattering cross section σ_p and rate for the production of CO within a 5-layers film of methanol condensed on an Ar spacer as a function of the incident electron energy. The dashed line is the intrinsic minimum rate of CO production due to the measurement at an incident electron energy of 14 eV [50].

$a^3\Pi$ of condensed CO shown as recorded for a 10 ML film of pure condensed CO in Fig 6,*b*.

In their first paper [50], Lepage, Michaud and Sanche demonstrated that the appearence of the CO electronic state derives exclusively from the electron induced fragmentation of condensed methanol molecules. Assuming a uniform electron current density within the electron beam, it can also be shown that for induced CO concentrations below 2%, an effective cross section for CO production σ_p, can be calculated via the formula

$$\sigma_p \cong \frac{n_{CO} S_0}{n_0 I_0 t} \qquad (7)$$

where I_0 is the incident electron beam current and S_0 its area; n_0 and n_{CO} are, respectively, the initial number density of target molecules and the number density of CO molecules at time t.

Figure 7 exhipits the incident electron energy dependence of the σ_p and CO production rate as a function of incident electron energy. The horizontal dashed line represents the intrinsic minimum rate of CO production due to the measurement of the energy loss spectra at 14 eV.

The CO production rate was found to increase linearly with the quantity of deposited methanol indicating that the CO is generated by the interaction of an electron at a single molecular site, rather than through reactions of fragment species with surrounding (intact) molecules. Processes that could produce CO thus include the following (calculated thermodynamic thresholds for each process are given in parentheses).

$$CH_3OH + e^- \rightarrow CH_3OH^+ + 2e^-$$

$$\rightarrow H^+ + CO + H_2 + H + 2e^-, \quad (18.87\ eV) \quad (8a)$$

$$\rightarrow H_2^+ + CO + H_2 + 2e^-, \quad (16.22\ eV) \quad (8b)$$

$$CH_3OH + e^- \rightarrow CH_3OH^- \rightarrow CH_3OH^* + e^-, \quad (8c)$$

$$CH_3OH^* \rightarrow CO + 4H, \quad (9.77\ eV) \quad (8d)$$

$$\rightarrow CO + H_2 + 2H, \quad (5.30\ eV) \quad (8e)$$

$$\rightarrow CO + 2H_2, \quad (0.80\ eV) \quad (8f)$$

$$CH_3OH + e^- \rightarrow CH_3OH^-$$

$$\rightarrow H^- + CO + 3H, \quad (8.97\ eV) \quad (8g)$$

$$\rightarrow H^- + CO + H_2 + H. \quad (4.50\ eV) \quad (8h)$$

Ionization processes (8a) and (8b) are not expected to contribute to the CO yield at incident electron energies below ~19 eV, while excitation of neutral repulsive states should produce a CO yield that increases linearly from threshold with E. Consequently, the shape of the CO yield function, visible in Fig. 7, was attributed to the formation of multiple transient anions at these low incident energies. In addition to DEA via long-lived resonances, (8g) and (8h), molecular dissociation is possible via shorter-lived states that decay to neutral repulsive states of CH_3OH. By comparison with H^- ESD yield functions [53] and vibrational excitation functions [54] for condensed CH_3OH, Lepage and co-authors ascribed the shoulder at 11.5 eV and broad maximum centered at 14.5 eV in Fig. 7 to the $...(6a')^1(3sa')^2$, ^2A, $...(1a'')^1(3sa')^2$, $^2A''$, and $...(5a')^1(3sa')^2$, $^2A'$ core excited electron resonances, which decay into their parent repulsive states. The rising signal above 19 eV was attributed to direct ionization of CH_3OH.

The same experimental techniques was applied to measure effective cross sections for the electron induced production of CO from condensed acetone [51]; the results are shown in Fig. 8. The energy dependence of the cross section by a threshold at 8 eV and strong rise to 14 eV, a broad maximum of $\sigma_p \sim$ $\sim 6.8 \cdot 10^{-17}$ cm^2 at 16 eV followed by a gradual and monotonic decrease to $\sim 4 \cdot 10^{-17}$ cm^2 at an energy of 25 eV. Again these measurements indicate that CO is generated by the fragmentation of single molecules by transient anion formation and decay via DEA and/or parent neutral repulsive states of acetone. Definitive statements on the anionic neutral

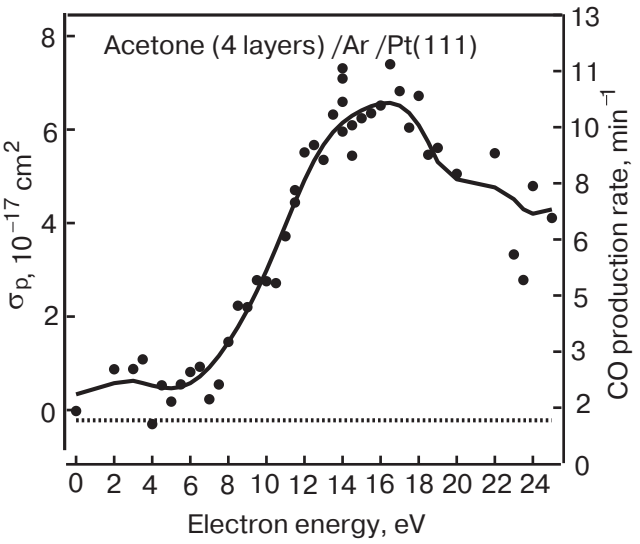

Fig. 8. Electron scattering cross section σ_p and rate for the production of CO within a four-layer film of acetone condensed on an Ar spacer as a function of the incident electron energy. The dashed line is the intrinsic minimum rate of CO production due to the measurement at an incident electron energy of 14 eV. The solid line is to guide the eye [51].

states involved in this process await further experimental measurements.

Dissociation of biomolecular targets

Considerable effort has been directed to understanding the genotoxic effects of low energy electrons in DNA. For example, recent experiments [55] have shown that electrons with energies < 5 eV are capable of inducing both single and double strand breaks in super-coiled plasmid DNA. Accurately identifying the mechanisms responsible for this damage requires complementary measurements on simpler molecular targets. The DNA molecule can be considered a molecular assembly consisting of two helical sugar-phosphate backbones, linked together by hydrogen-bonded base pairs (adenine «A» and thymine «T», cytosine «Cy» and guanine «G») and covered by water molecules. Consequently, understanding can be gained by electron impact experiments with these individual sub-units. Of these, condensed water has received the widest attention and our work in this area can be found in reference [56] together with references to earlier work. Here we briefly describe recent studies of electron impact on condensed dioxyribose analogues [57,58] and DNA bases [59].

Figure 9 shows the H^- ESD yield functions from multilayer tetrahydrofuran (I), 3-hydroxytetrahydrofuran (II) and α-tetrahydrofurfuryl alcohol (III), together with the chemical identities of these three compounds. These latter were selected for study because of

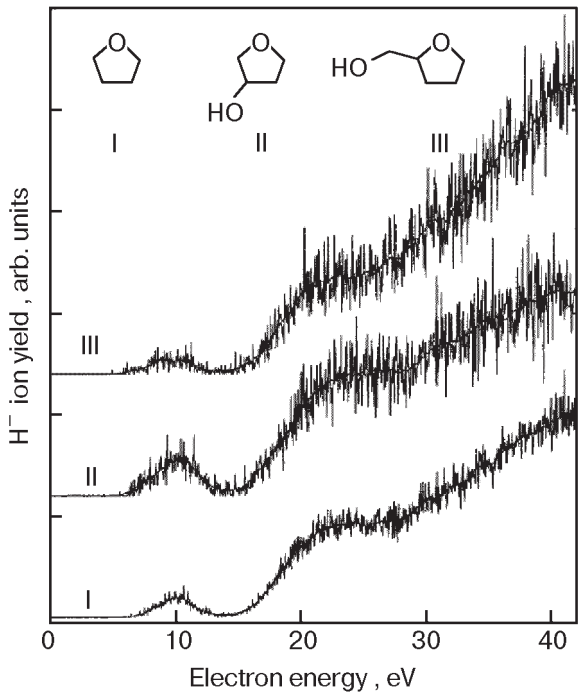

Fig. 9. Comparisons of H- ESD yields produced by impact of 0 to 40-eV electrons on 6-ML-thick films of the DNA backbone sugarlike analogues tetrahydrofuran (I), 3-hydroxytetrahydrofuran (II), and α-tetrahydrofurfuryl alcohol (III). The smooth solid lines serve as guides to the eye [58].

structural similarities with the sugar-like elements of the DNA backbone. For each compound, only H^- was found to desorb under electron impact [57,58]. Similarly, the H^- yield functions for each molecule show a broad peak at 10 eV which arises from selective dissociation of the C—H bonds, and is typical of DEA to hydrocarbon molecules. A second lower-energy resonance near 7.3 eV in II (just visible in the figure), correlated well with a Feshbach resonance observed in solid methanol [60,61] and so was attributed to the DEA to the OH substituent. However, no similar Feshbach resonance was observed in the H^- ESD yield from III.

Also apparent in the yield functions of Fig. 9 are broad structures near 23 eV. Measurements of the H^- signal at this energy as a function of coverage of I, II, and III on Ar spacer films [58], show that the 23 eV structure can not be attributed to multiple scattering by incident electrons, but rather to the formation of a resonance lying above the DD threshold. This latter thus decays into an electronic state (or states) that dissociates into H^- and the corresponding positive ion radical.

Electron impact experiments have also been performed on condensed DNA bases [59] and Fig. 10 presents the ESD signal of stable anions desorbed from ~ 8 ML thick films of adenine, thymine, guanine, and cytosine by a 500 nA beam of 20 eV electrons.

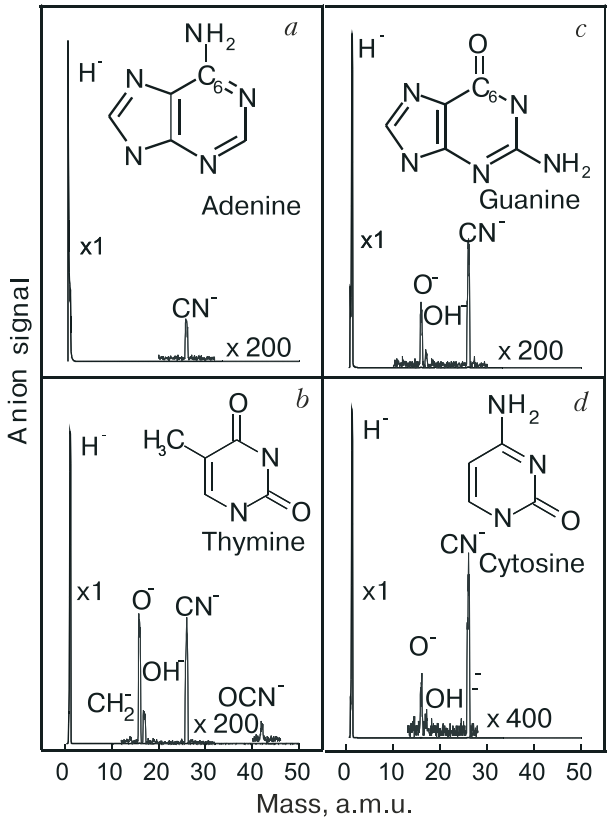

Fig. 10. Masses of stable anions desorbing from 8 monolayers (ML) thick films of adenine (*a*), thymine (*b*), guanine (*c*), and cytosine (*d*) bombarded by a 500 nA beam current of 20 eV electrons. The chemical structure of each molecule is also given [59].

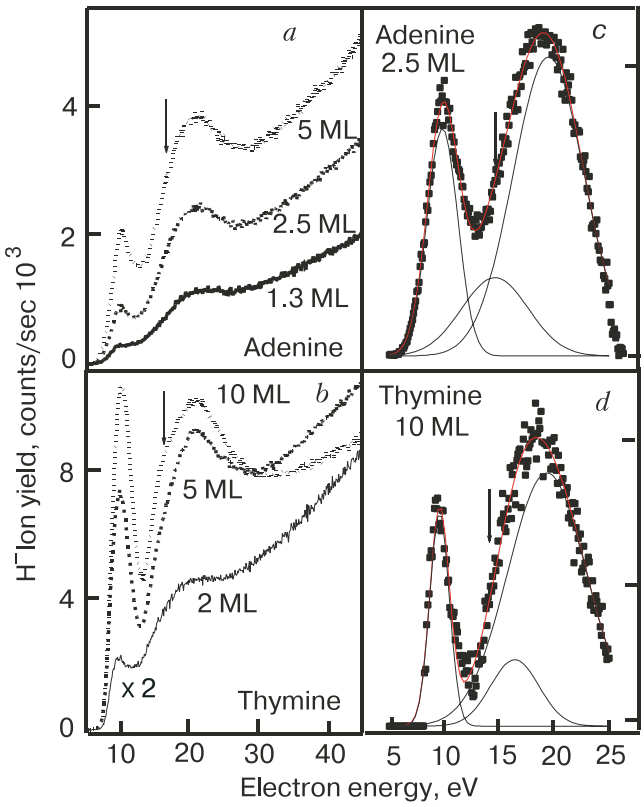

Fig. 11. Electron energy dependence of the H^- ion yield desorbed from adenine (*a*) and thymine (*b*), for different film thicknesses or exposure. The arrow indicates the shoulder observed at 14–15 eV incident electron energy. The yield functions of adenine (*c*) and thymine (*d*) are obtained by subtracting a linear background from (*a*) and (*b*), respectively [59].

Also shown are the chemical identities of these four molecules. The figure demonstrates that in addition to H^- (which is by far the strongest anion signal), electron bombardment produces CN^-, O^- and OH^- (except for adenine that does not contain O), and CH_2^-, and OCN^- (only in the case of thymine). Figure 11 presents H^- yield functions for varying quantities of condensed adenine (*a*) and thymine (*b*) obtained using a 6 nA electron beam. Curves (*c*) and (*d*) were obtained by subtracting a background that increases linearly with energy above a threshold at 10 eV. Readily apparent in both yield functions are two structures at 10 and 20 eV. These are more clearly seen once the background has been subtracted, as is a weak shoulder at 15 eV. The anion yield functions can be effectively fit using three gaussian functions of widths 3–5 eV at energies close to 10, 15 and 20 eV.

According to *ab initio* calculations [62] transient anion formation at 8–9 eV and at 14–15 eV in thymine and adenine can be attributed to electron capture by the positive electron affinity of excited states involving excitation of the lone pair $n \to \pi^*$, $\pi \to \pi^*$ and /or $\sigma \to \sigma^*$. Formation of H^- at these energies is likely to occur via dissociation of a core-excited resonance. Furthermore, comparison with gas-phase experiments [63] indicates that H^- production near 10 eV arises from C–H bond cleavage. As with tetrahydrofuran and its derivatives [57,58], the features at 20 eV are ascribed to the formation of a transient anion and its decay into a dissociative neutral state.

As seen in Fig. 10, at 500 nA incident electron currents, weak desorbed signal of heavier anions fragments are observable. Anion yield functions for each fragment were measured and Fig. 12 shows, as an example of such data, the various CN^- yield functions obtained for the four DNA bases. Once more the curves display large irregular variations which at energies below ~ 15 eV can be attributed to molecular fragmentation via DEA.

Sharp resonance features in the CN^- yield functions at 9–10 eV (depending on molecule) are degenerate with similar structures in the appropriate CH_2^-, OCN^-, O^- and OH^- yield functions, suggesting that they arise from the formation of the same excited isocyanic anion intermediate $(OCNH)^{*-}$, via closely lying but distinct resonances; i.e., (G^-, Cy^-, or T^-) $\to$

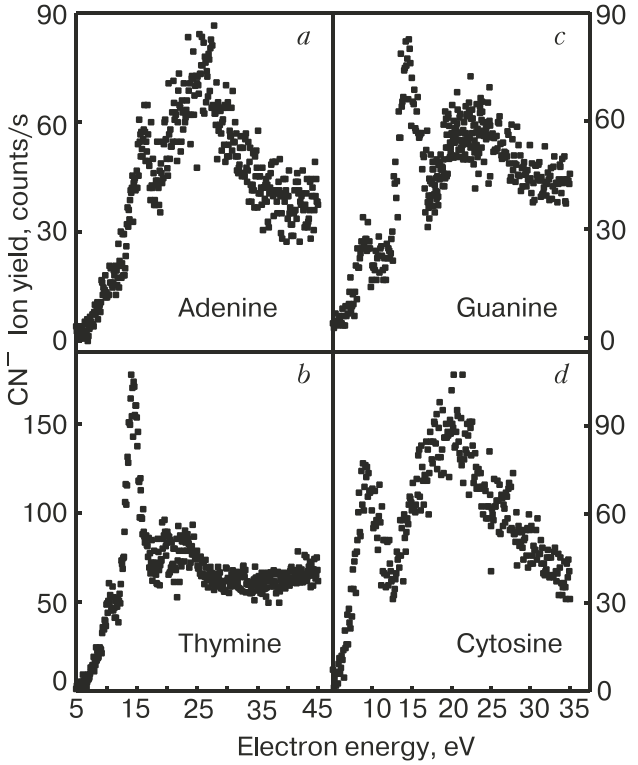

Fig. 12. Incident electron energy dependence of CN^- ion yields desorbed under 500 nA electron bombardment of 8 ML thick films of adenine (*a*), thymine (*b*), guanine (*c*), and cytosine (*d*) [59].

$\rightarrow R + (OCNH)^{*-}$, where $(OCNH)^{*-}$ further undergoes fragmentation into different possible dissociative channels: $CN^- + (O+H)$, $OH^- + CN$ or $O^- + (CNH)$. Alternatively, the coincidence of the peak at 9.0 and 10 eV in the yield function of CN^-, OH^- and O^- ions from Cy or G and T, respectively, may indicate that they are induced via a single predissociative resonance, as suggested in the case of gas phase bromouracil [64]. Such a mechanism would then involve a crossing or saddle point in the multi-dimensional potential energy surface of the electronically excited state of cytosine, guanine or thymine anions, along the OCN^--(radical), O^--(radical) and CN^--(radical) coordinates. However, irrespective of the detailed dissociation mechanisms, the desorption of these heavier anions demonstrates that, apart from exocyclic rupture of C–H bonds, low energy electrons can initiate complex multi-bond ring dissociation.

5. Reactions initiated following dissociation

Reactive scattering

Reactive scattering by DEA fragment ions in condensed media was first noted in the form of OH^- electron stimulated desorption yields from O_2 embedded in multi-layer alkane films [65] and subsequently for aniline physisorbed on top of O_2 solids [66]. The O^- anion produced following DEA to N_2O has also been observed to react with other N_2O molecules within an Ar/N_2O matrix, to generate a desorbed yield of NO^- and NO_2^-, among other products [67]. Part of the H_2 ESD yield observed from multilayer films of H_2O, at incident electron energies below 10 eV, has also been attributed to proton abstraction by DEA H^- fragments, viz. $H^- + H_2O \rightarrow \{H_3O\}^{*-} \rightarrow H_2 + OH^-$ [68], and has thus been associated with part of the unscavengeable H_2 yield formed in water radiolysis [69]. Another (post-DEA) ion-molecule reaction directly observed in the condensed phase for ion kinetic energies well below 5 eV, is isotope exchange measured in $^{18}O_2/C^{16}O$ mixed solids [70], i.e., $^{18}O^- + C^{16}O \rightarrow \{C\,^{18}O^{16}O\}^{*-} \rightarrow {}^{16}O^- + C^{18}O$. Formation of D_2O in synchrotron irradiated films of N_2O has also been attributed to associative electron attachment reactions of DEA O^- fragments with matrix D_2 molecules, i.e., $O^- + D_2 \rightarrow D_2O^{*-} \rightarrow D_2O + e^-$ [71]. Measurements of electron stimulated O_3 production in condensed O_2 films were attributed to post dissociation reactions of neutral $O(^3P$, or $^1D)$ with adjacent molecules [72]. The threshold energy for this process being near 3.5 eV, allowed DEA to be identified as the source of $O(^3P)$ at low incident electron energies. Similarly, Azria and co-workers in their measurements of F^- and Cl^- desorption from condensed CF_2Cl_2 [73] have have observed the appeance of new features in the Cl^- yield function at long bombardment times. These changes were attributed to the synthesis of Cl_2 in the condensed phase by an as yet unidentified reaction pathway having DEA to CF_2Cl_2 as it's initial step. More recently, Tegeder and Illenburger [74], have shown by comparison of anion ESD data and infrared-absorption-reflection spectroscopy that DEA is the initial step in the production of N_2F_4 molecules within NF_3 films under bombardment with 0 to 5 eV electrons.

In our initial studies of anion desorption from solid O_2/hydrocarbon mixtures [65] several observations were made concerning the desorbed signal of OH^-. (1) The OH^- yield functions resembled more closely the yield functions of O^- with $E_k \geq 1.5$ eV from pure O_2 films, than the H^- signal associated with DEA to the hydrocarbon molecule. (2) The OH^- signal from an O_2 film increases linearly with alkane surface coverage below 1 ML, and (3) the threshold in energy for OH^- desorption coincided with that for O^- desorption, which is at least 2 eV below the H^- desorption onset. For these reasons, and the fact that O_2^- is the only charged product observed in the gas-phase collisions of H^- with O_2 [75], the OH^-

desorption signal was attributed to hydrogen abstraction reactions of the type

$$O^- + C_nH_m \rightarrow C_nH_mO^{*-} \rightarrow OH^- + C_nH_{m-1}.$$

The existence of such a $C_nH_mO^{*-}$ intermediate anion collision complex had previously been suggested by Comer and Schulz [76], who measured the energies of electrons emitted during gas-phase collisions of O^- with C_2H_4. Further evidence for a complex anion formation and reactive scattering in the gas phase can be seen in the studies of Parkes [77] and Lindinger [78].

More recent measurements [79] reproduced in Fig.13 show an enhanced H^- signal *at low E* from the O_2/C_4H_{10} mixed films which varies greatly with film composition. Two trends can be observed in Fig 13,*a* with increasing O_2 concentration. Firstly, there is a decrease in the yield of H^- at 10 eV, the peak energy of H^- production via direct DEA to the alkane molecule. Secondly, there is the appearance and development of a second H^- ESD structure at lower energies, such that at an O_2 concentration of 20% a substantial fraction of the H^- yield occurs *at incident electron energies significantly below those required for DEA to* C_4H_{10}. In Fig. 13,*b* the H^- yield function from a *n*-butane film containing 10% O_2 by volume (curve *1*) is resolved into two separate components. One, located at 10 eV, is assumed identical in form to that of H^- desorption from pure C_4H_{10}. The other (bold curve *2*) is obtained from curve *1* when the H^- signal from a pure film normalized to curve *1* at 10 eV (dotted line) is removed. This procedure yields a second quasi-gaussian shaped structure centered at 7.8 eV, close to the energy of maximum production of O^- via DEA and with a threshold at 5.5 eV, identical to that observed for OH^- production. From these observations, the increase in H^- production at incident electron energies below the threshold for DEA to C_4H_{10} was attributed to reactive scattering of O^- ion and atom-exchange reactions of the type,

$$O^- + C_4H_{10} \rightarrow C_4H_{10}O^{*-} \rightarrow H^- + C_4H_9O$$

involving the same or similar transient anions as those responsible for OH^- production. Evidence for additional channels in the decay of such $C_nH_mO^{*-}$ anions was apparent in the anion yield functions of CH^- and CH_2^- from thin films of C_2H_4/O_2 mixtures [79] as a sub-direct DEA threshold component to the anion signals.

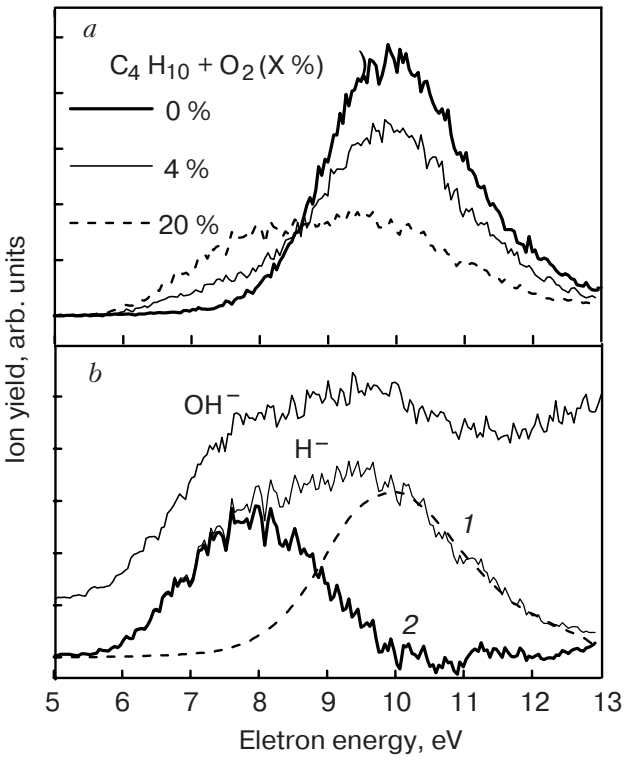

Fig. 13. (*a*) The H^- yield function from 4 ML thick films of a O_2/C_4H_{10} mixture of increasing percentage volume concentration of O_2. (*b*) The H^- signal from a 4 ML thick mixture of 10% O_2 in C_4H_{10}, can be resolved into two components: one centered at 10 eV, associated with H^- production via DEA to the alkane (dotted line) and another at 7.8 eV, associated with reactive scattering of O^- ions (bold line). Also shown is the yield of OH^- ions from the same film [79].

Electron induced reactions of adsorbates and substrates

X-ray photoelectron spectroscopy has been used to analyze modifications induced by 2 to 20 eV electrons incident on a hydrogen passivated and sputtered Si(111) surface, onto which had been *physisorbed* thin films of H_2O [80,81] and CF_4 [82]. In both cases following the electron-induced dissociation of the molecular adsorbate, a new XPS signal associated with the *chemisorption* of either O or F onto the Si surface was observed. Cross sections for this process can be obtained from the relation,

$$I(\Phi) = I(\infty)[1 - \exp(-\sigma_{CH}\,\Phi/A)], \qquad (9)$$

Here, $I(\Phi)$ represents the energy integrated intensity of the XPS chemisorption feature following a dose of Φ electrons over an area A of the sample, $I(\infty)$ is the (saturated) signal at high doses and σ_{CH} is the cross section for the chemisorption reaction.

The effective cross section for electron induced chemisorption of oxygen from a H_2O bilayer, onto a hydrogen passivated Si(111) surface is shown in Fig.14 as a function of incident electron energy [80,81]. The data were obtained by monitoring the evolution of a chemisorbed O 1*s* in XPS spectra and subsequent fitting to Eq. (9). The low energetic threshold for the

chemisorption process (i.e., 5.2 eV) has been interpreted as due to the formation of OH via the DEA process

$$H_2O[X] + e^- \leftrightarrow H_2O^-[^2B_1, A_1] \rightarrow$$

$$\rightarrow H^-[^2S_0] + OH[^2\Pi]$$

and its subsequent reaction with the surface, viz.,

$$Si_3 - Si - H + OH \rightarrow Si_3 - Si - OH + H.$$

The chemisorption process has its maximum cross section at ~ 11 eV in contrast with cross sections for the radiolysis of bulk ice. This difference was understood as being dependent on the selective quenching of dissociative electronic states of water due to the resonant charge exchange between the substrate and adsorbate and the absence of multiple inelastic scattering in the H_2O bilayer on Si(111) [80,81].

A similar XPS study has been performed for ~ 1 ML of CF_4 deposited onto the same hydrogen passivated Si substrate [82], the results of which are shown in Fig. 15. Comparisons with gas phase results [83] and with measurements of ESD [84] and charge trapping cross section [85] (this latter is included in Fig. 15), clearly demonstrate that for this molecule the chemisorption of F^- containing species is dependent on the DEA reactions

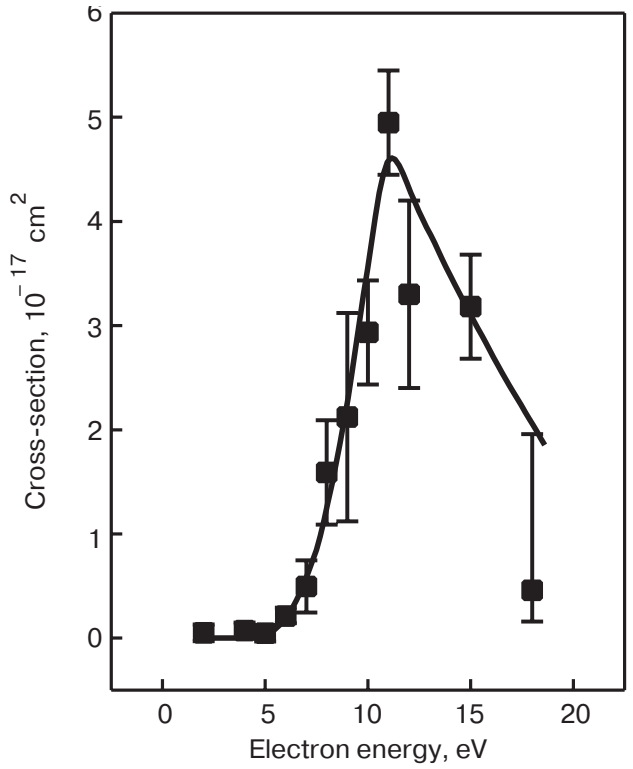

Fig. 14. Experimental cross sections for the electron induced oxidation of the a-H:Si(111) surface as a function of incident electron energy as obtained in Ref. 80, 81. The solid line is drawn to guide the eye.

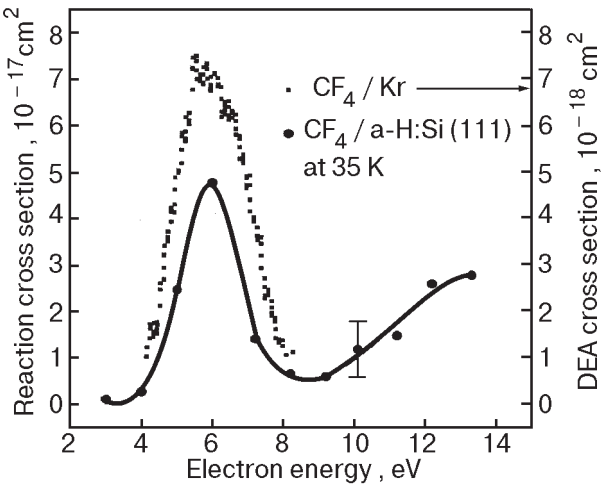

Fig. 15. Experimental cross section for the electron induced reaction of H:Si(111) surface with physisorbed CF_4 as a function of electron energy [82]. The solid line is drawn to guide the eye. Also shown is the total DEA cross section for CF_4 on Kr, as measured by Bass et al. [85].

$$CF_4 + e^- \rightarrow CF_4 \rightarrow F^- + CF_3,$$

$$CF_4 + e^- \rightarrow CF_4 \rightarrow F + CF_3^-$$

as a initial step to further reactions of fragments with the Si substrate.

6. Conclusions

The data presented in this article illustrate how cryogenics and electron impact techniques may be used to study electron-driven reactions in a number of molecular solid and adsorbate/substrate systems. The simplicity of the experimental approach has allowed certain general observations to be made.

At incident electron energies below ~ 20 eV, the formation of transient negative ions plays an important role in molecular dissociation, via DEA and/or populating neutral dissociative states.

The DEA and ESD processes are affected by environmental factors such film morphology and composition, which can modulate electron scattering prior to electron attachment and/or affect molecular fragments after dissociation.

Electron-induced dissociation is a general process observed even for multilayer films of molecules of biological significance such as tetrahydrofuran and the DNA bases.

Dissociation may involve significant molecular rearrangement, sufficient to break apart cyclic molecules.

Molecular fragment species may react with surrounding molecules or with a supporting substrate.

From the wide range of molecular solids investigated, it has been shown that the combination of cryogenic techniques and electron impact methods can provide meaningful information for understanding radiation and particle beam induced damage in the molecular components of DNA as well as other simpler systems. Such a comprehension has applications (or implications) for diverse fields, ranging from, the electron-beam modification of organic SAMS [3] to ozone depletion [86,87]. Unsurprisingly, there is also much current interest in using this experimental approach to mimic conditions in space and so investigate radiation induced chemistry occurring at the surfaces of various heavenly bodies [88].

In the future, electron-impact measurements will be extended to solid targets of progressively greater molecular complexity (i.e., large polymeric materials such as proteins) or compositional complexity (i.e., solids containing more than one or two chemical components). Greater emphasis will also likely be placed on following the reactive steps succeeding electron induced dissociation, using techniques such as HREELS, and so trace the relationship between the initial products of electron impact (or irradiation, etc.,) and those observed at long times.

Acknowledgments

We gratefully acknowledge the cooperation and contributions of many colleagues in Sherbrooke and elsewhere, without whom this work was not have been possible. This research was supported by the Canadian Institutes of Health Research and by the National Cancer Institute of Canada.

1. L Sanche, *IEEE Trans. Electrical Insulation* **28**, 789 (1993)
2. Jong-Liang Lin, C. Singh Bhatia, and John T. Yates, Jr., *J., Vac. Sci. Technol*. **A13,** 163 (1995); Jong-Liang Lin and John T. Yates, Jr. *J. Vac. Sci. Technol*. **A13**, 1867 (1995)
3. S. Frey, K. Heister, M. Zharnikov, and M. Grunze, *Phys. Chem. Chem. Phys*. **2**, 1979 (2000); J.E. Hernandez, H. Ahn, and J.E. Whitten *J. Phys. Chem.* **B105**, 8339 (2001).
4. D. Syomin, J. Kim, B.E. Koel, and G.B.Ellison, *J. Phys. Chem*. **B105**, 8387 (2001).
5. V. Cobut, Y. Frongillo, J.P. Patau, T. Goulet, M.-J. Fraser, and J.-P. Jay-Gerin, *Radiat. Phys. Chem*. **51,** 229 (1998).
6. L. Sanche, *Scanning Microscopy* **9**, 619 (1995).
7. A.D. Bass and L. Sanche, *Radiat. Environ. Biophys*. **37**, 243 (1998).
8. L. Sanche, *Surf. Sci*. **451**, 81 (2000).
9. J. Franck and G. Hertz, *Verhand. Deut. Physik Ges*. **16**, 512 (1914).
10. G.J. Schulz, *Rev. Mod. Phys*. **45,** 378 (1973).
11. G. F. Hanne, *Am. J. Phys*. **56**, 696 (1988).
12. P.Rowntree, H. Sambe, L. Parenteau, and L. Sanche, *Phys. Rev*. **B47,** 4537 (1993).
13. L. Sanche, *J. Phys*. **C13**, L677 (1980).
14. Ph. Avouris and R.E. Walkup, *Annu. Rev. Phys. Chem*. **40,** 173 (1989).
15. T.F. O'Malley, *Phys. Rev*. **150,** 14 (1966).
16. L. Sanche, *J. Chem. Phys*. **71**, 4860 (1979).
17. G. Perluzzo, G. Bader, L.G. Caron, and L. Sanche, *Phys. Rev. Lett*. **55**, 545 (1985).
18. M.-A. Hervé du Penhoat, M.A. Huels, P. Cloutier, J.-P. Jay-Gerin, and L. Sanche, J. Chem. Phys. **114**, 5755 (2001).
19. M.A. Huels, L. Parenteau, and L. Sanche, *J. Chem. Phys*. **100**, 3940 (1994).
20. S. Wurm, P. Feulner, and D. Menzel, *Surf. Sci*. **400**, 155 (1998); M. Scheuer, D. Menzel, and P. Feulner, *Surf. Sci*. **390**, 23 (1997).
21. G.A. Kimmel, T.M. Orlando, C. Vezina, and L. Sanche, *J. Chem. Phys*. **101**, 3282 (1994); G.A. Kimmel and T.M. Orlando, *Phys. Rev. Letts*. **75**, 2606 (1995).
22. T.D. Harries, D.H. Lee, M.Q. Blumberg, and C.R. Arumainaygam, *J. Phys. Chem*. **99**, 9530 (1995).
23. For example: P. Rowntree, C. Dugal, D. Hunting, and L. Sanche *J. Phys. Chem*. **100**, 4546 (1996); H. Abdoul-Carime, P.-C. Dugal and L. Sanche, *Radiat. Res*. **153**, 23 (2000) (and references therein).
24. G. Leclerc, A.D. Bass, A. Mann, and L. Sanche, *Phys. Rev.* **B46**, 4865 1992.
25. A. Stomatovic and G.J. Schulz, *Rev. Sci. Instrum*. **41**, 423 (1970).
26. R.M. Marsolais, M. Deschenes, and L. Sanche, *Rev. Sci. Instrum*. **60**, 2724 (1989).
27. K. Nagesha, J. Gamache, A.D. Bass, and L. Sanche, *Rev. Sci. Instrum*. **68**, 3883 (1997).
28. M. Michaud and L. Sanche, *Phys. Rev*. **B30**, 6067 (1984).
29. M. Michaud, P. Cloutier, and L. Sanche, *Rev. Sci. Instrum*. **66**, 2661 (1995).
30. D. Briggs and M.P. Seah, *Pratical Surface Analysis, Auger and X-ray Photoelectron Spectroscopy* 2nd, D. Briggs and M.P. Seah (Eds.) John Wiley, Chichister, U.K., Vol. 1 (1990).
31. L. Sanche, *Phys. Rev. Lett*. **53**, 1638 (1984).
32. R.J. Van Brunt and L.J. Kieffer, *Phys. Rev.* **A2,** 1899 (1970).
33. R. Azria, L. Parenteau, and L. Sanche, *Phys. Rev. Lett*. **59**, 638 (1987).
34. M.N. Hedhili, L. Parenteau, M.A. Huels, R. Azria, M. Tronc, and L. Sanche, *J. Chem. Phys*. **107**, 7577 (1997).
35. K.P. Stevenson, G.A. Gimmel, Z Dohnalek, R.S. Smith, and B.D. Kay, *Science* **283,** 1501 (1999); P. Ayotte, R. Scott Smith, K.P. Stevenson, Z. Dohnálek, G.A. Kimmel, and B.D. Kay, *J. Geophys. Res*. **106**, 33387 (2001) (and references therein).
36. E. Vichnevetski, A.D. Bass, and L. Sanche, *J. Chem. Phys*. **113**, 3874 (2000).

37. R. Azria, Y. LeCoat, M. Lachgar, M. Tronc, L. Parenteau, and L. Sanche, *Surf. Sci*. **436**, L671 (1999); *ibid*. **451**, 91 (2000).
38. A.D. Bass, L. Parenteau, F. Weik, and L. Sanche, *J. Chem. Phys*. **115**, 4811 (2001).
39. L. Sanche, A.D. Bass, P. Ayotte, and I.I. Fabrikant, *Phys. Rev. Lett*. **75**, 3568 (1995).
40. P. Ayotte, J. Gamache, A.D. Bass, I.I. Fabrikant, and L. Sanche, *J. Chem. Phys*. **106**, 749 (1997).
41. P. Rowntree, L. Sanche, L. Parenteau, M. Meinke, F. Weik, and E. Illenberger, *J. Chem. Phys*. **101**, 4248 (1994).
42. D.M. Pearl and P.D. Burrow, *Chem. Phys. Lett*. **206**, 483 (1993).
43. M. Michaud and L. Sanche, *J. Elect. Spectrosc. Rel. Phenom.* **51**, 237 (1990).
44. I.I. Fabrikant, *J. Phys.* **B24**, 2213 (1991); *J. Phys*. **B27,** 4325 (1994).
45. I.I. Fabrikant, K. Nagesha, R. Wilde, and L. Sanche, *Phys. Rev.* **B56**, R5725 (1997).
46. D.M. Pearl and P.D. Burrow, *J. Chem. Phys*. **101,** 2940 (1994); K. Aflatooni and P.D. Burrow, *J. Chem. Phys*. **113**, 1455 (2000).
47. D.M. Pearl, P.D. Burrow, I.I. Fabrikant, and G.A. Gallup, *J. Chem. Phys*. **102,** 2737 (1995).
48. K. Nagesha and L. Sanche, *Phys. Rev. Lett*. **78**, 4725 (1997).
49. K. Nagesha, I.I. Fabrikant, and L. Sanche, *J. Chem. Phys*. **114**, 4934 (2001).
50. M. Lepage, M. Michaud, and L. Sanche, *J. Chem. Phys*. **107**, 3478 (1997).
51. M. Lepage, M. Michaud, and L. Sanche, *J. Chem. Phys*. **113**, 3602 (2000).
52. R. Martel, A. Rochefort, and P.H. McBreen, *J. Am. Chem. Soc*. **116**, 5965 (1994).
53. L. Parenteau, J.-P. Jay-Gerin, and L. Sanche, *J. Phys. Chem*. **98,** 10277 (1994).
54. A.T. Wen, M. Michaud, and L. Sanche, *Phys. Rev*. **A54**, 4162 (1996); A.T. Wen, M. Michaud, and L. Sanche, *J. Electron Spectrosc. Rel. Phenom*. **94**, 23 (1998).
55. B. Boudaiffa, P. Cloutier, D. Hunting, M.A. Huels, and L. Sanche, *Science* **287**, 1658 (2000).
56. W.C. Simpson, M.T. Sieger, G.A. Kimmell, K. Nagesha, L. Parenteau, T.M. Orlando, and L. Sanche *J. Chem. Phys*. **108**, 5027 (1998); W.C. Simpson, M.T. Sieger, G.A. Kimmel, L. Parenteau, L. Sanche, and T.M. Orlando, *J. Chem. Phys*. **107**, 8668 (1997).
57. D. Antic, L. Parenteau, M. Lepage, and L. Sanche, *J. Phys. Chem*. **B103**, 6611 (1999).
58. D. Antic, L. Parenteau, and L. Sanche, *J. Phys. Chem*. **B104,** 4711 (2000).
59. H. Abdoul-Carime, P. Cloutier, and L. Sanche, *Radiat. Res*. **155,** 625, (2001).
60. M. Michaud, M.-J. Fraser, and L. Sanche, *J. Chem. Phys*. **91,** 1223 (1994).
61. L. Parenteau, J.-P. Jay-Gerin, and L. Sanche, *J. Phys. Chem*. **98**, 10277 (1994).
62. S. Peng, A. Padva, and P.R. LeBreton, *Proc. Natl., Acad. Sci. USA* **73,** 2966 (1976); C. Yu, S. Peng, I. Akiyama, J. Lin, and P.R. LeBreton, *J. Am. Chem Soc*. **100,** 2303 (1978); J. Lin, C. Yu, S. Peng, I. Akiyama, K. Li, Li Kao Lee, and P.R. LeBreton, *J. Phys. Chem.* **84**, 1006 (1980).
63. M.A. Huels, I. Hahndorf, E. Illenburger, and L. Sanche, *J. Chem. Phys*. **108**, 1309 (1998).
64. H. Abdoul-Carime, M.A. Huels, F. Bruning, E. Illenberger, and L. Sanche, *J. Chem. Phys.* **113**, 2517 (2000).
65. L. Sanche and L. Parenteau, *Phys. Rev. Lett*. **59**, 136 (1987); *J. Chem. Phys*. **93**, 7476 (1990).
66. M.A. Huels, L. Parenteau, and L. Sanche, *Chem. Phys. Lett.* **279**, 223 (1998).
67. L. Sanche and L. Parenteau, *J. Chem. Phys*. **90**, 3402 (1989).
68. G.A. Kimmel, T.M. Orlando, C. Vezina, and L. Sanche**,** *J. Chem. Phys*. **101**, 3282 (1994).
69. V. Cobut, J.-P. Jay-Gerin, Y. Frongillo, and J.P. Patau, *Radiat. Phys. Chem*. **47**, 247 (1996).
70. R. Azria, L. Parenteau, and L. Sanche, *Chem. Phys. Lett*. **171**, 229 (1990).
71. D.M. Hanson, *Abstracts of the 46th Annual Meeting of the Radiat. Res. Soc*. Louisville, KY (1998), p. 86.
72. S. Lacombe, F. Cemic, K. Jacobi, M. N. Hedhili, Y. Le Coat, R. Azria, and M. Tronc, *Phys. Rev. Lett*. **79**, 1146 (1997).
73. M.N. Hedhili, M. Lachgar, Y. Le Coat, R. Azria, M. Tronc, Q.B. Lu, and T.E. Madey, *J. Chem. Phys*. **114**, 1844, (2001).
74. P. Tegeder and E. Illenberger, *Chem. Phys. Lett*. **341**, 401 (2001).
75. M.S. Huq, L.D. Doverspike, and R.L. Champion, *Phys. Rev*. **A27**, 785 (1983).
76. J. Comer and G.L. Schulz, *Phys. Rev*. **A10,** 2100 (1974).
77. D.A. Parkes, *J. Chem. Soc Faraday Trans*. **I68** 613 (1972).
78. W. Lindinger, D.L. Albritton, F.C. Fehsenfeld, and E.E. Fergusson, *J. Chem. Phys*. **63**, 3238 (1975).
79. A.D. Bass, L. Parenteau, M. A. Huels, and L. Sanche, *J. Chem. Phys*. **109**, 8635 **(**1998).
80. D. Klyachko, P. Rowntree, and L. Sanche, *Surf. Sci*. **346**, L49 (1996).
81. D. Klyachko, P. Rowntree, and L. Sanche, *Surf. Sci*. **389**, 29 (1997).
82. W. Di, P. Rowntree, and L. Sanche, *Phys. Rev*. **B52**, 16618 (1995).
83. T. Oster, A. Kuhn, and E. Illenberger, *Int. J. Mass Spectrom. Ion Processes* **89**, 1 (1989).
84. M. Meinke, L. Parenteau, P. Rowntree, L. Sanche, and E. Illenberger, *Chem. Phys. Lett*. **205**, 213 (1993).
85. A.D. Bass, J. Gamache, L. Parenteau, and L. Sanche, *J. Phys. Chem*. **99**, 6123 (1995).
86. Q.-B. Lu and L. Sanche *Phys. Rev. Lett*. **87**, 078501 (2001).
87. Q.B. Lu and L. Sanche, *Phys. Rev*. **B63**, 153403 (2001).
88. T.E. Madey, R.E. Johnson, and T.M. Orlando, *Surf. Sci*. **500**, 838 (2002).